Title
Temperature Variation of the Local Structure and Dihydrogen Bonds in Ammonia Borane

Author(s)
Kazutaka Ikeda / Yoshihiro Shimizu / Tessui Nakagawa / Akihiko Machida / Hyunjeong Kim / Kouji Sakaki / OHARA Koji / Hidetoshi Ohshita / Toshiya Otomo

Journal
Journal of the American Chemical Society 147 (25) , 21803 - 21810

Published
2025-05-14

URL (The Version of Record)
https://doi.org/10.1021/jacs.5c04566

Temperature Variation of Local Structure and Dihydrogen Bonds in Ammonia Borane

Kazutaka Ikeda[†,*], Yoshihiro Shimizu[‡], Tessui Nakagawa[‡], Akihiko Machida[§], Hyunjeong Kim[¶], Kouji Sakaki[¶], Koji Ohara[⊥], Hidetoshi Ohshita[#], Toshiya Otomo[#]

[†] Neutron Industrial Application Promotion Center, Comprehensive Research Organization for Science and Society (CROSS), Tokai, Ibaraki 319-1106, Japan

[‡] Faculty of Science, University of the Ryukyus, Senbaru, Nishihara, Okinawa 903-0213, Japan

[§] Quantum Beam Science Research Directorate, National Institutes for Quantum Science and Technology, Sayo, Hyogo 679-5148, Japan

[¶] National Institute of Advanced Industrial Science and Technology, Tsukuba, Ibaraki 305-8569, Japan

[⊥] Faculty of Materials for Energy, Shimane University, Nishi-Kawatsu-Cho, Matsue Shimane 690-8504, Japan

[#] Institute of Materials Structure Science, High Energy Accelerator Research Organization (KEK), Tokai, Ibaraki 319-1106, Japan

ABSTRACT: Because ammonia borane (AB) exhibits a high hydrogen storage density derived from dihydrogen bonds, it has the potential to be a safe, lightweight, and compact hydrogen storage material. In the tetragonal phase at around room temperature, the hydrogen occupancy is low and the atomic arrangement and electron density distribution have not been clarified. Therefore, the hydrogen storage properties, including the decomposition reaction mechanism, which proceeds from ~373 K, also remain unclear. In this study, neutron/X-ray total scattering measurements were performed on AB above and below its phase-transition temperature of 225 K, and the disordered atomic arrangement of hydrogen in the tetragonal phase was clarified by reverse Monte Carlo modeling of the obtained pair distribution function. In addition, the charge of each atom was quantitatively investigated by first-principles calculations and Bader charge analysis. Hydrogen in AB was orderly arranged, forming $N–H^{\delta+}\cdots H^{\delta-}–B$ dihydrogen bonds in the low-temperature orthorhombic phase; however, in the room-temperature tetragonal phase, where the hydrogen atoms were disorderly arranged, the distribution of negatively charged hydrido-like $H^{\delta-}$ atoms coordinated to boron extended toward neutral. This situation shows that the dihydrogen bonds are unstable, which may lead to decomposition of AB.

INTRODUCTION

Hydrogen energy is an inevitable option for the energy shift underway worldwide. Efficient, safe, economical, and compact hydrogen storage technology is critical for the use of hydrogen as a renewable energy source, especially for fuel cell vehicles, which absolutely require the ability to carry hydrogen at a high gravimetric and volumetric density and to absorb and release hydrogen at a sufficiently high rate.[1, 2] Among the various hydrogen storage materials (e.g., metal/alloy hydrides, complex hydrides, metal–organic frameworks, and carbon- and chemical-based materials) that have been proposed, ammonia borane (AB, NH_3BH_3) has attracted attention as a hydrogen storage material because of its high hydrogen density (gravimetric and volumetric hydrogen densities of 190 g/kg and 100–140 g/L, respectively).[3, 4]

The decomposition reaction of AB proceeds from ~373 K, which is close to its melting point (~383 K).[5-7] This melting point is substantially higher than that of ethane (CH_3CH_3, 92 K), which has a molecular structure similar to that of AB, and the dihydrogen bond connecting adjacent molecules in AB is thought to be responsible for its high thermodynamic stability.[3] The crystal structure of AB transforms from a low-temperature orthorhombic phase ($Pmn2_1$; no. 31) to a room-temperature tetragonal phase ($I4mm$; no. 107) at ~225 K.[8] X-ray and neutron diffraction measurements have shown that both phases contain two molecules of AB in the unit cell and that the lattice parameters and lattice volume increase continuously with increasing temperature.[9] The crystal structure and molecular orientation of the orthorhombic phase have been studied in detail, revealing that hydrogen occupies a special crystallographic position.[10] The B–N bonds form layers parallel to the *c*-axis, where the B–N bonds are alternately inclined toward the *c*-axis. The hydrogen–hydrogen distance is inferred to indicate the formation of dihydrogen bonds (0.202 nm), which are shorter than the total van der Waals radius of hydrogen (0.24 nm),[11] and the deuterium positions determined from neutron diffraction (ND) measurements confirmed the actual short interatomic distances.[9, 12] The B–N bond layers are also present in the tetragonal phase; however, the B–N bonds are aligned four-fold to the *c*-axis. The AB molecules rotate around the B–N bond parallel to the *c*-axis, with N as the fulcrum. At the same time, the crystal lattice contracts in the *a*-axis direction but expands in the *b*-axis direction, eventually transitioning to the tetragonal phase. Although the intramolecular geometry is almost unaffected by this process, the hydrogen bonding is substantially diminished in the tetragonal phase. Researchers have speculated that a further temper-

ature increase would weaken this bonding and lead to hydrogen release.[3]

The actual hydrogen–hydrogen distance in the tetragonal phase has not been reported previously, presumably because the atomic arrangement of the tetragonal phase is disordered, and the hydrogen-occupied sites are accompanied by vacancies. For the crystal structure thus experimentally obtained, ab initio calculations using the generalized gradient approximation yielded an excessively large unit-cell volume for AB and inappropriate lattice constants; however, introducing van der Waals forces through semiempirical corrections greatly improved the cell parameters and intermolecular geometry, and charge transfer from NH_3 to BH_3 for dihydrogen bonds in the orthorhombic phase was shown.[13-16] By contrast, the presence of dihydrogen bonds has not been clarified in the tetragonal phase because unambiguously determining whether hydrogen or vacancies are present in sites with a low hydrogen occupancy of only one-quarter is difficult.[15]

For AB and its derivatives to be used as hydrogen storage materials, it is necessary to clarify the atomic arrangement and electron density distribution in the tetragonal phase, which is closely related to the room-temperature hydrogen storage properties and to the slow hydrogen release reaction that occurs at ~373 K. Because average structure-based analyses such as Rietveld refinement are insufficient to reveal disordered atomic arrangements such as tetragonal phases with stochastic atomic positions, large atomic ensembles without space-group symmetry are required. Therefore, in the present study, the atomic arrangement of the disordered structure in the tetragonal phase is clarified by reverse Monte Carlo (RMC) modeling of the pair distribution function (PDF) obtained from neutron/X-ray total scattering measurements, and the charge of each atom is quantitatively investigated by first-principles calculations and Bader charge analysis.[17] The results provide insights into the hydrogen storage properties of AB and enable an analysis of the local structure of hydrogen and the temperature dependence of dihydrogen bonds.

MATERIALS AND METHODS

Sample Preparation. $ND_3{}^{11}BD_3$ enriched with D and ^{11}B instead of H and B in NH_3BH_3, respectively, was prepared via the following procedure because the neutron incoherent scattering cross section of D is smaller than that of H ($\sigma_{inc}{}^{H}$: 80.27, $\sigma_{inc}{}^{D}$: 2.05×10^{-28} m^2) and because the neutron absorption cross section of ^{11}B is substantially smaller than that of ^{10}B ($\sigma_{abs}{}^{B}$: 767, $\sigma_{abs}{}^{10B}$: 3835, $\sigma_{abs}{}^{11B}$: 0.0055×10^{-28} m^2 at 1.8 Å neutron).[18] $Na^{11}BD_4$ powder (Katchem spol. s r. o., Czech Republic, 96.8% pure) was dissolved in tetrahydrofuran and subsequently mixed with $(NH_4)_2SO_4$. The mixture was stirred at 313 K for 24 h in the presence of molecular sieves to remove water. The solution after the reaction was filtered and then evaporated under vacuum at 313 K to obtain a powder. These procedures were carried out in a glovebox filled with Ar with O_2 and H_2O contents less than 0.5 ppm. The obtained powder was dissolved in D_2O under air to exchange N–H for N–D bonding, and the resultant solution was evaporated to dryness using an evaporator. Sample purity with small amounts of BHD_2, BH_2D, and BH_3 and extremely small amounts of NH_3 was confirmed via ^{11}B, ^{11}B–H decoupling, and ^{1}H NMR experiments. To minimize (hydro-)oxidation or nitrogenation, the sample was handled in a glovebox filled with purified He with an O_2 content less than 1 ppm and a dew point less than 183 K after the preparation.

X-ray and Neutron Total Scattering Measurements. $ND_3{}^{11}BD_3$ powders were loaded into a polyimide film tube with an inner diameter of 1 mm and a thickness of 0.05 mm in a glovebox. Synchrotron X-ray total scattering measurements were performed using a Rigaku R-AXIS V detector at beamline BL22XU at SPring-8. Scattering data for $ND_3{}^{11}BD_3$ at 100, 200, 250, and 300 K were collected over a lattice spacing range of 0.03–0.65 nm for XRD with an incident energy of 69.6 keV (wavelength of 0.0178 nm). The raw data were corrected for polarization, absorption, and background, and the contribution from Compton scattering was subtracted from the scattering data to obtain the X-ray static structure factor $S(Q)$.[19]

The $ND_3{}^{11}BD_3$ powders sealed in a V–Ni null scattering sample container with an outer diameter of 6.0 mm and a thickness of 0.1 mm in a glovebox, and neutron total scattering measurements were performed at 20, 100, 200, 250, and 300 K, each for an exposure time of 3 h. These measurements were conducted using a NOVA neutron total scattering instrument (beamline BL21) with a decoupled liquid hydrogen moderator, an incident flight path of 15 m, and a scattered flight path of 1.2–1.3 m at the 90° detector bank ($d = 2\pi/Q = \lambda/(2\sin\theta) = 0.008$–$0.63$ nm) connected to an 800 kW spallation neutron source in the Materials and Life Science Experimental Facility (MLF) of the Japan Proton Accelerator Research Complex (J-PARC). The background intensities of the sample container and instrument were subtracted from the scattering data, and the neutron attenuation factors for the sample and sample containers were calibrated to obtain the neutron structure factor $S(Q)$.[19]

Structural refinements of the ND patterns for the $ND_3{}^{11}BD_3$ sample at 20, 100, 200, 250, and 300 K in reciprocal space were performed by Rietveld refinement using the computer program Z-Rietveld (ver. 2.1.3).[20,21] Fourier transform of the X-ray $S(Q)$ for the $ND_3{}^{11}BD_3$ sample was performed in the Q_{min} to Q_{max} range $1.0 \leqq Q \leqq 200.0$ nm^{-1} to obtain the PDF, $g(r)$,[22] using the Orochi program suite.[23] For the $g(r)$ for the neutron $S(Q)$, the range $9.0 \leqq Q \leqq 300.0$ nm^{-1} was used for the Fourier transformation. The neutron PDFs were refined with the software PDFgui (ver. 2.0.4).[24]

Reverse Monte Carlo Modeling. The atomic arrangements for the orthorhombic and tetragonal phases of $ND_3{}^{11}BD_3$ were investigated by fitting the $S(Q)$ and the corresponding $g(r)$ using GSAS-II[25] in tandem with RMCProfile (ver. 6.7.9). [26] The method used 12 × 12 × 12 or 4 × 4 × 4 superlattices for the RMCProfile structural modeling using $S(Q)$ and $g(r)$. Initial structures were created, where each atom was randomly placed to match the aforementioned Rietveld refinement results, and the $S(Q)$ and $g(r)$ were reproduced by modeling. In the modeling of the orthorhombic phase, only translation of each constituent atom (N, B, and D) from the sites of the refined crystal structure was attempted. Because the hydrogen and vacancies in the superlattices created in the modeling preparation are randomly arranged in the tetragonal crystal with low occupancy of hydrogen-occupied sites, we attempted to reproduce $S(Q)$ and $g(r)$ obtained from the experiment by swapping D and vacancies with probabilities of 0.6 and simultaneously translating the constituent atoms with probabilities of 0.4. The maximum translations were restricted to 0.001 nm for N and B and to 0.010 nm for D. These values were determined from the magnitude of the atomic displacements obtained from the Rietveld and PDF refinement results. The N, B, and D atoms were constrained to move no closer than the predefined cutoff distance of 0.08 nm.

First-Principles Density Functional Theory Calculations. We investigated the electron density distribution of NH_3BH_3 using a self-consistent-field run of first-principles density functional theory (DFT) calculations as implemented in the Vienna Ab initio Simulation Package (VASP)[27,28] with a plane-wave basis and the projector augmented wave method[29,30] within the generalized gradient approximation with the Perdew–Burke–Ernzerhof exchange-correlation functional.[31] A cutoff energy of 400 eV was used throughout. To emphasize the atomic arrangement derived from the RMC modeling, structural optimization by VASP was not performed. Although a larger ensemble of atoms is desirable to reproduce the experimental results, self-consistent field (SCF) calculations were performed on the 4 × 4 × 4 superlattices obtained from the aforementioned RMC modeling because the DFT calculation requires a substantial amount of time. The criterion for self-consistency in the electronic structure determination was that two consecutive energies differ by less than 0.1 meV. The *k*-point spacing was ~0.02 nm^{-1}.

RESULTS AND DISCUSSION

Refinements of Neutron Diffraction Patterns and Pair Distribution Functions. The structural phase-transition temperature of ND_3BD_3 shifts to 1.5 K higher than that of NH_3BH_3, and the deuterium substitution reduces the enthalpy variation from 1.29 to 1.01 kJ/mol by more than 20%; however, the respective symmetries of the crystal structures below and above the transition temperature are not changed by hydrogen isotopes.[32] The neutron diffraction pattern of $ND_3{}^{11}BD_3$ was refined by the Rietveld method and, as previously reported,[10] converged to the orthorhombic phase ($Pmn2_1$) at 20, 100, and 200 K and to the tetragonal phase ($I4mm$) at 250 and 300 K (Figs. S1(a) and 1(a), Table S1(a)). The impurities detected by NMR did not affect the refinement results. The 200 K refinement result has a slightly larger reliability factor than the others, which might indicate contamination by intermediate phases that form near the phase-transition temperature.[33] The reported PDF for $ND_3{}^{11}BD_3$ does not show the refinement results because of the presence of a small amount of hydrogen from the incomplete deuteration of the sample.[10] The PDFs derived from the neutron total scattering measurements were refined as single phases to the orthorhombic and tetragonal phases below and above 225 K, respectively, similar to the results of the crystal structure analysis (Fig. S1(b), Table S1(b)). The lattice constants and lattice volumes obtained from this structural information increased continuously with increasing temperature, in relatively good agreement with previously reported results; however, the lattice constants and lattice volumes at 300 K were slightly larger than those previously reported (Fig. S2(a)(b)).[10] In the orthorhombic phase, as in the previous report,[10] the B–N tilted from the *c*-axis of the unit cell becomes progressively parallel as the temperature increases from the lowest temperature to the phase-transition temperature.

As shown in Tables S1(a) and S1(b), in the tetragonal phase, the deuterium distributed around the B and N of the B–N along the *c*-axis occupies one-quarter of the 8*d* and 16*e* sites. For the atomic pair correlations obtained from the Rietveld and PDF refinements, the temperature variation of the B–N, B–D, and N–D bond lengths were relatively small and close to previously reported values;[10] however, at 300 K, the B–N and N–D bond lengths were slightly larger than previously reported values, as were the corresponding lattice parameters and volume (Fig. S2(c)). The distances of B–D correlations at temperatures greater than the phase-transition temperature deviated from the Rietveld refinement and PDF refinement results. Regarding the deuterium–deuterium correlation, the D_{B1}–D_{N2} bond lengths increased with increasing temperature in the tetragonal phase and shortened when the temperature was greater than the phase-transition temperature (Fig. S2(d)), consistent with previously reported results.[10] The D_{B2}–D_{N1} bond lengths showed little change with temperature, including temperatures above and below the phase-transition temperature. Although the D_{B2}–D_{N2} correlation distance increased at temperatures greater than the phase-transition temperature in the previous report,[10] it decreased in the present study. The discontinuous change in D_{B2}–D_{N2} is unnatural, in contrast to the continuous change in lattice constants and other parameters below and above the phase-transition temperature. Because the hydrogen occupancy in the tetragonal phase is 1/4 of the 8*d* and 16*e* sites, and because the two shortest occupied sites are unlikely to be simultaneously occupied by two hydrogens, discussing the shortest correlation distance on the basis of the average structure is difficult; however, the second- and third-nearest neighbor sites are assumed to correspond to the actual pair correlation.[34] Thus, the Rietveld refinement, which imposes symmetry constraints on the structure by long-range averaging, is limited in its ability to elucidate disordered atomic arrangements in crystal structures.[10] Therefore, as previously reported, the actual atomic arrangement in the tetragonal phase could not be reproduced and the dihydrogen bond changes over a wide temperature range, including the phase transitions, could not be studied from the viewpoint of the average structure.

Reverse Monte Carlo Modeling. RMC modeling for the 12 × 12 × 12 superlattices ($N_{3456}D_{10368}B_{3456}D_{10368}$ at 20, 100, and 200 K, $N_{3456}D_{10420}B_{3456}D_{10301}$ at 250 K, and $N_{3456}D_{10384}B_{3456}D_{10509}$ at 300 K) was performed using the neutron and X-ray total scattering PDF and static structure factor $S(Q)$ for $ND_3{}^{11}BD_3$, which converged well, as shown in Fig. S3(a)–(d). When the unit cell was extended to create the superlattice, some atoms from sites with low occupancy near the boundaries were missing, resulting in a deviation from the stoichiometric composition. The modeling was performed using a combination of neutron and X-ray total scattering data acquired at 100, 200, 250, and 300 K, whereas data acquired at 20 K were modeled using neutron total scattering data alone. Because AB is composed of relatively light elements, X-ray total scattering data are also useful for such structural analysis and can supplement neutron total scattering data. In addition, the modeling was performed for the 4 × 4 × 4 superlattices ($N_{128}H_{384}B_{128}H_{384}$ at 20, 100, and 200 K and $N_{128}H_{370}B_{128}H_{370}$ at 250 and 300 K).

As shown in Fig. 1(b), when the atomic arrangement of the 4 × 4 × 4 superlattices is projected onto the unit cell, partial correlations are revealed, enabling nitrogen-coordinated deuterium, D_N, and boron-coordinated deuterium, D_B, to be distinguished. As shown in Fig. 2, the N–N, B–B, N–B, and N–D correlations do not substantially vary with temperature in the range from 20 to 300 K; however, at lower temperatures, correlations remain at distances longer than $r > 0.2$ nm, indicating that thermal fluctuations of each atom are suppressed. By contrast, for the B–D correlation, the distance for the orthorhombic phase decreased as the temperature increased from 20 to 200 K and did not substantially change after the transition to the tetragonal phase at 225 K. The distribution of N–D and B–D correlations showed a continuous trend across the phase-transition temperature.

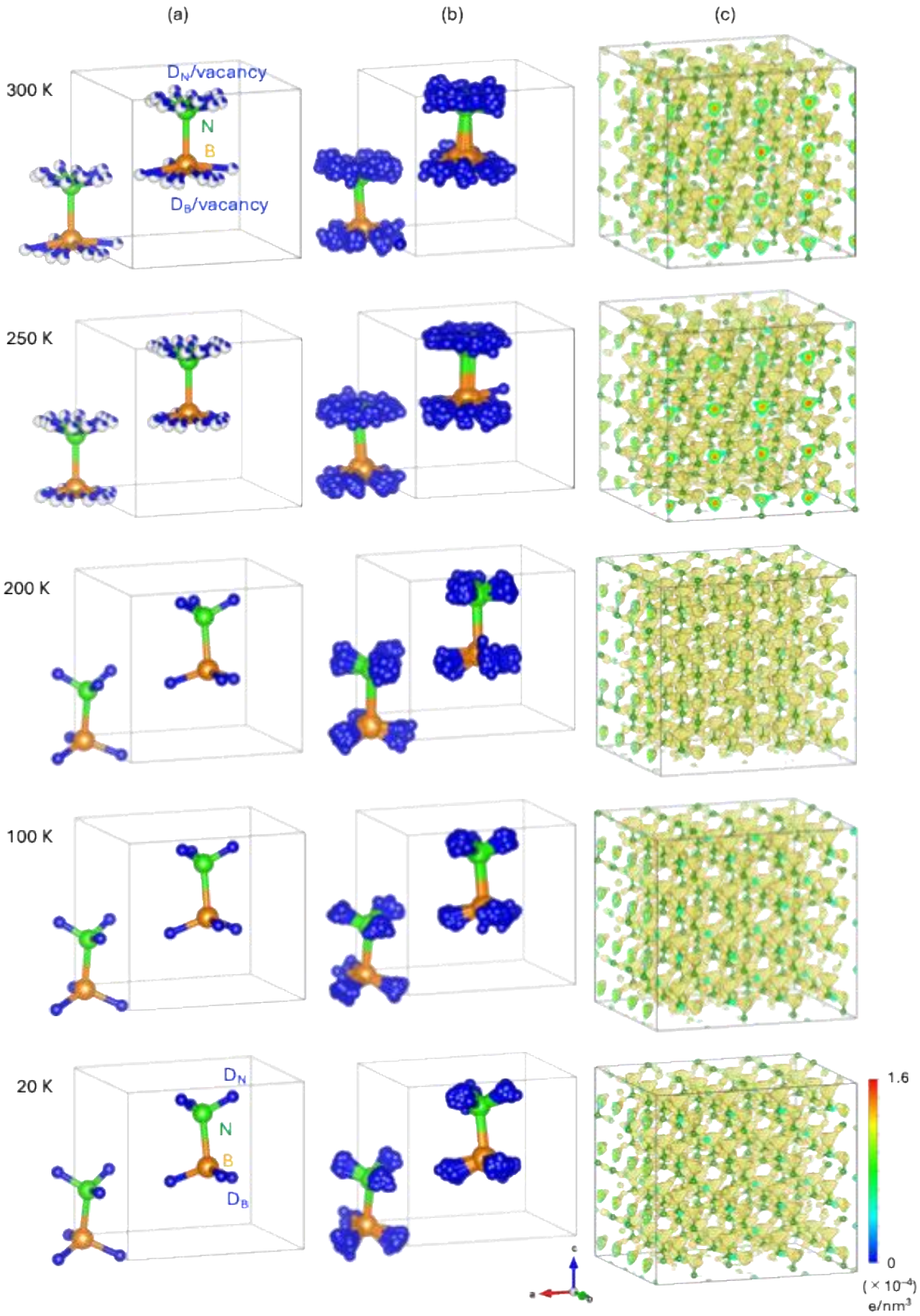

Figure 1. (a) Crystal structures and (b) atomic arrangements of $ND_3{}^{11}BD_3$, and (c) charge densities of NH_3BH_3 at 20, 100, 200, 250, and 300 K. Crystal structures with space group $Pmn2_1$ (No. 31) below 225 K and $I4mm$ (No. 107) above 225 K were obtained from Rietveld refinements. Atomic arrangements were obtained from RMC modeling. The positions in the atomic arrangements are indicated by the projection of the 4 × 4 × 4 superlattices onto the unit cell for the RMC modeling results. Charge densities of the 4 × 4 × 4 superlattices were obtained from Bader charge analysis.

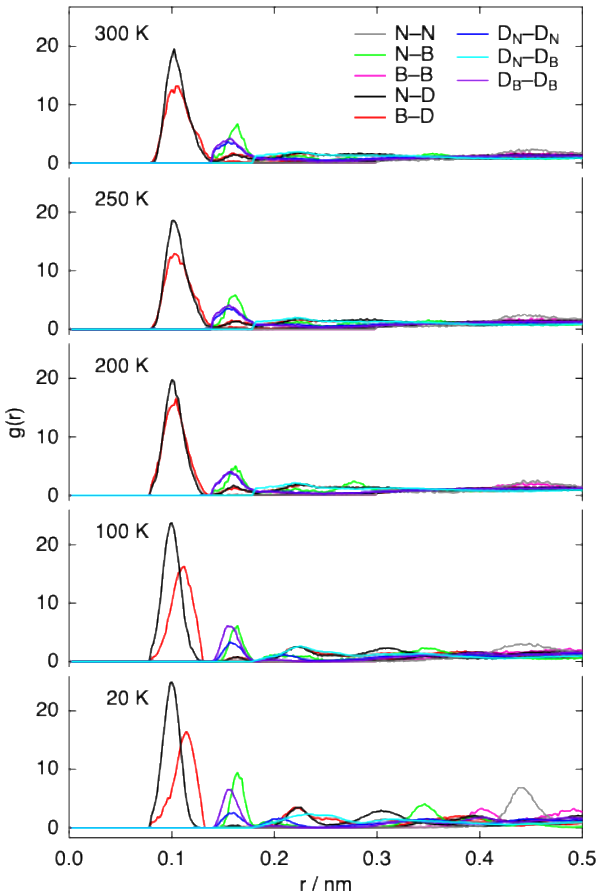

Figure 2. Partial PDF profiles of $ND_3{}^{11}BD_3$ at 20, 100, 200, 250, and 300 K, as obtained from RMC modeling of the 12 × 12 × 12 superlattices.

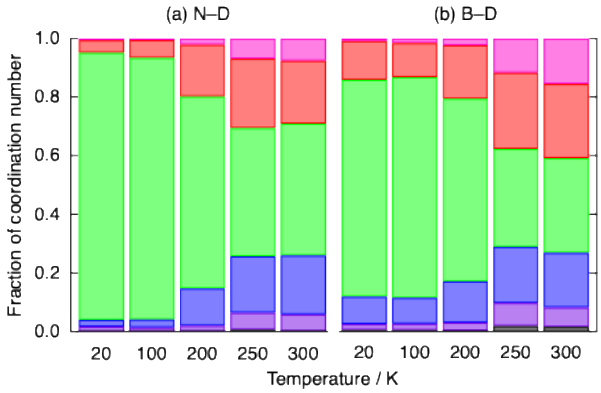

Figure 3. Fraction of D coordination number for (a) N and (b) B in $ND_3{}^{11}BD_3$ at 20, 100, 200, 250, and 300 K, as obtained from RMC modeling. Coordination numbers: 0 (black), 1 (purple), 2 (blue), 3 (green), 4 (red), and 5 (magenta).

The fractions of D coordinating to N and B obtained from the RMC modeling are shown in Fig. 3. In the low-temperature orthorhombic phase, most N atoms have a coordination number of 3. From near the phase-transition temperature to room temperature, the fraction of N atoms with a coordination number of 3 decreases from 90% to approximately 50%, and that of N atoms with a coordination number of 2 or 4 increases to 20%. Three-quarters of B atoms have a coordination number of 3 in the orthorhombic phase, and from near the phase-transition temperature to room temperature, the fractions of B atoms with coordination numbers of 2, 3, and 4 are approximately one-third each. During the decomposition process of AB at ~373 K, other chemical species such as diammoniate of diborane ($[NH_3BH_2NH_3]^+[BH_4]^-$; DADB), have been detected by ^{11}B magic-angle spinning (MAS) NMR in the first stage of hydrogen release after an induction period,[35,36] consistent with the results obtained from RMC modeling, where fewer D atoms are coordinated to B than to N at around room temperature. The short-range intramolecular correlations of D_N–D_N and D_B–D_B are particularly clear at all temperatures, indicating that the average molecular structure is maintained. Unlike the average structure results from the Rietveld and PDFfit methods, the D_N–D_B correlation shows little temperature variation with respect to the number and distance of nearest-neighbor correlations and is continuous, including at temperatures below and above the phase-transition temperature. That is, hydrogen in AB undergoing thermal vibrations is not present at some specific sites in the crystal structure (e.g., the 8*d* and 16*e* sites in *I*4*mm*); however, it is distributed around the circumference of the base of the cone with N or B at the apex while maintaining the molecular structure.

DFT Calculations and Bader Charge Analysis. As compared in Fig. S4, the number of atoms in the 4 × 4 × 4 superlattice is 1/27 the number in the 12 × 12 × 12 superlattice, which reduces the statistical precision of the partial correlations obtained from the RMC modeling and makes discussing the shape of the atomic distribution difficult; however, the tendencies of each atomic correlation are similar. To complete the first-principles calculations in a realistic time frame, we carried out SCF calculations using VASP on the basis of the atomic arrangement derived by RMC modeling of 4 × 4 × 4 superlattices (Fig. 1(c)). VESTA was used for the three-dimensional display of the charges.[37] In the orthorhombic phase at 20 K, there is a higher density of electrons in the N-coordinated hydrogen, H_N, than in the B-coordinated hydrogen, H_B, and the shape of the equipotential surface is similar to a regular tetrahedron. In addition, NH_3BH_3 molecules with the same direction of H_N and H_B and the same shape of the equipotential surface of electron density are orderly arranged. In the region below the phase-transition temperature, the shape of the equipotential surface and the orientation of the molecules are gradually disordered with increasing temperature. In the tetragonal phase above the phase-transition temperature, the shape of the equipotential surface and the orientation of the molecules are further disordered. At 300 K, the electron density of H_B is substantially reduced and the equipotential surface of H_N is considerably deformed from a tetrahedron. These effects correspond to the broadening of the N–D and B–D distance distributions and to the changes in the coordination number obtained from the RMC modeling (Figs. 2 and 3).

The charges attributed to each element were quantitatively evaluated via Bader charge analysis.[17] This analytical technique can estimate the chemical state of the constituent atoms from the atomic arrangement of AB to integrate the charge for each atom with respect to the charge gradient (Fig. 4).[38] The weighted valence of the constituent atoms can also be estimated from the atomic number, charge, and core electron number (valences of N = 7 − charge + 2, B = 5 − charge + 2, and H = 1 − charge), as shown in Table 1. The valences are larger in absolute value than the respective charges derived from the previously reported Born effective charge analysis;[16] however, Bader charge analysis has been noted to give more appropriate results for covalent materials.[39]

The results show a distribution of protonate-like $H^{\delta+}$, in which H_N atoms are positively charged, and hydrido-like $H^{\delta-}$, in which H_B atoms are negatively charged. The resultant N–$H^{\delta+}\cdots H^{\delta-}$–B dihydrogen bond stabilizes the AB molecule as a solid. Therefore, the formation of dihydrogen bonds was quantitatively confirmed by the atomic arrangement based on the experimental results. In the orthorhombic phase at temperatures below 225 K, the charge distribution of all of the elements is small, indicating the formation of stable hydrides. By contrast, in the tetragonal phase at temperatures above 225 K, the atomic distribution of hydrogen becomes more disordered; the charge distribution of H_B, in particular, broadens toward neutral, suggesting destabilization of the dihydrogen bonds. Presumably, the valence distribution of nitrogen and boron broadens towards negative with this change in H_B valence; however, the reason for the small change in the H_N valence is unknown.

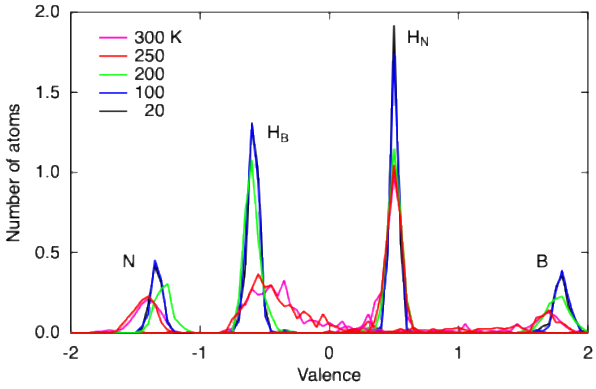

Figure 4. Valence distribution of NH_3BH_3; the distribution was obtained from DFT calculations and Bader charge analysis based on the atomic arrangement of $ND_3{}^{11}BD_3$ at 20, 100, 200, 250, and 300 K, as obtained from RMC modeling.

Various AB-based materials have been reported as hydrogen storage materials (e.g., $LiNH_2BH_3$, $NaNH_2BH_3$, and NaH–NH_3BH_3).[40-42] For example, the addition of LiH or $LiNH_2$ promotes the decomposition reaction of AB.[43] $LiNH_2BH_3$ also suppresses the release of volatile gases that are harmful to polymer-electrolyte fuel cells, releasing 15.6 wt% hydrogen at 363 K.[44] Because the local structure and electron density distribution of ABs are assumed to be changed by additives, resulting in changes in ABs' hydrogen release properties, further development of the present method is expected to provide useful knowledge for the development of hydrogen storage materials. By contrast, multiple hydrogen chemical states exist in $LaMg_2NiH_7$, and the changes in hydrogen density are accompanied by progressive transitions in the hydrogen chemical states.[45, 46] To understand the complex hydrogen absorption and desorption reactions and develop materials with high hydrogen storage density, it is important to understand the relationship between hydrogen chemical states and hydrogen storage reactions; the present method is effective for clarifying this relationship.

Table 1. Weighted Valences of the Constituent Atoms Obtained by Bader Charge Analysis; Standard Deviations Are in Parentheses and Refer to the Last Digit

Phase	Temp. / K	N	H_N	B	H_B
*I*4*mm*	300	–1.42(4)	0.45(14)	1.27(2)	–0.40(7)
	250	–1.44(4)	0.46(14)	1.34(2)	–0.43(7)
*Pmn*2$_1$	200	–1.28(5)	0.47(15)	1.76(4)	–0.63(14)
	100	–1.34(6)	0.47(19)	1.80(5)	–0.62(17)
	20	–1.34(5)	0.47(20)	1.79(5)	–0.62(17)
	(ref.[16])	–0.78	0.22	0.83	–0.22
			0.25		–0.28

CONCLUSION

Although the crystal structure of the low-temperature orthorhombic phase has been previously investigated by neutron or X-ray diffraction measurements of AB and the Rietveld refinement method, the hydrogen positions in the room-temperature tetragonal phase were stochastic (site occupancies of one-quarter); thus, the actual atomic arrangement of hydrogen was unclear. In the present study, an ensemble of approximately 1,000 atoms that simultaneously satisfy the diffraction patterns and PDFs obtained by complementary total scattering measurements of neutrons and X-rays was obtained by RMC modeling to derive all atomic configurations including hydrogen, and the electron density distribution and valence of each atom were evaluated by first-principles calculations based on this ensemble. The charge distribution of AB shows that, in the orthorhombic phase at temperatures below the phase-transition temperature, a N–$H^{\delta+}\cdots H^{\delta-}$–B dihydrogen bond was stably formed. By contrast, in the tetragonal phase at temperatures above the phase-transition temperature, the distribution of hydrido-like $H^{\delta-}$ with negatively charged hydrogen atoms coordinated to boron extends toward neutrality, suggesting that the decomposition reaction proceeds from some unstable dihydrogen bonds.

ASSOCIATED CONTENT

Supporting Information

The Supporting Information is available free of charge on the ACS Publications website.

Table S1. Results of (a) Rietveld and (b) PDF refinements with space group *Pmn*2$_1$ (no. 31) and *I*4*mm* (no. 107) of $ND_3{}^{11}BD_3$ at 20, 100, 200, 250, and 300 K, as obtained via neutron scattering measurements. *g*: Occupancy, *U*: isotropic atomic displacement, R_{wp}, R_F, and R_w: weighted reliability. Standard deviations are in parentheses and refer to the last digit. Parameters without standard deviations were fixed in the refinement. Atomic displacements of D were assumed to be the same for the Rietveld refinements.

Figure S1. (a) Powder diffraction and (b) PDF profiles for $ND_3{}^{11}BD_3$ at 20, 100, 200, 250, and 300 K, as obtained via neutron total scattering measurements. Rietveld and PDF refinement results: observed (black), calculated (red), and residual (blue) profiles.

Figure S2. (a) Lattice parameters, (b) lattice volume, (c) bond lengths of B–N, B–D, and N–D, and (d) bond lengths for D–D of $ND_3{}^{11}BD_3$ at 20, 100, 200, 250, and 300 K, as obtained from Rietveld and PDF refinements of neutron diffraction and total scattering measurements.

Figure S3. RMC modeling results for (a) neutron PDF, (b) neutron $S(Q)$, (c) X-ray PDF, and (d) X-ray $S(Q)$ of $ND_3{}^{11}BD_3$ at 20, 100, 200, 250, and 300 K. RMC modeling results: observed (black), calculated (red), and residual (blue) diffraction and PDF profiles.

Figure S4. Partial PDF profiles for $ND_3{}^{11}BD_3$ at 20, 100, 200, 250, and 300 K, as obtained from RMC modeling on the 4 × 4 × 4 superlattices.

AUTHOR INFORMATION

Corresponding Author

* k_ikeda@cross.or.jp

Present Addresses

‡ Faculty of Advanced Science and Technology, Ryukoku University, 1-5 Yokotani, Seta Oe-cho, Otsu, Shiga 520-2194, Japan; shimizu@rins.ryukoku.ac.jp

Author Contributions

The final manuscript includes contributions from all authors.

Funding Sources

This work was supported in part by GteX Program Japan Grant Number JPMJGX23H1 and a project, JPNPP20003, commissioned by the New Energy and Industrial Technology Development Organization (NEDO).

Notes

The authors declare no competing financial interest.

ACKNOWLEDGMENT

We acknowledge Dr. Hiroyuki Saitoh of National Institutes for Quantum Science and Technology for useful discussions on local structure analysis of X-ray total scattering data. The synchrotron radiation experiments were performed at JAEA beamline BL22XU of SPring-8 with the approval of the Japan Synchrotron Radiation Research Institute (JASRI) [proposal numbers 2022B3751 and 2023A3751]. The neutron total scattering experiments were approved by the Neutron Scattering Program Advisory Committee [proposal numbers 2014S06 and 2019S06].

ABBREVIATIONS

AB, ammonia borane; RMC, reverse Monte Carlo; DFT, density functional theory; SCF, self-consistent field.

REFERENCES

(1) Tarhan, C.; Çil, M. A. A study on hydrogen, the clean energy of the future: Hydrogen storage methods. Journal of Energy Storage 2021, 40. DOI: 10.1016/j.est.2021.102676.

(2) Wang, G.; Luo, Z.; Desta, H. G.; Chen, M.; Dong, Y.; Lin, B. AI-driven development of high-performance solid-state hydrogen storage. Energy Reviews 2025, 4 (1). DOI: 10.1016/j.enrev.2024.100106.

(3) Staubitz, A.; Robertson, A. P. M.; Ianners, I. Ammonia-Borane and Related Compounds as Dihydrogen Sources. Chem. Rev. 2010, 110, 45. DOI: 10.1021/cr100088b.

(4) Hassan, I. A.; Ramadan, H. S.; Saleh, M. A.; Hissel, D. Hydrogen storage technologies for stationary and mobile applications: Review, analysis and perspectives. Renewable and Sustainable Energy Reviews 2021, 149. DOI: 10.1016/j.rser.2021.111311.

(5) Burnett, L. J.; Muller, B. H. Melting points of ethane and three of its deuterated modifications. Journal of Chemical & Engineering Data 2002, 15 (1), 154-157. DOI: 10.1021/je60044a013.

(6) Himmelberger, D. W.; Alden, L. R.; Bluhm, M. E.; Sneddon, L. G. Ammonia borane hydrogen release in ionic liquids. Inorg. Chem. 2009, 48 (20), 9883-9889. DOI: 10.1021/ic901560h.

(7) Zhong, R. Q.; Zou, R. Q.; Nakagawa, T.; Janicke, M.; Semelsberger, T. A.; Burrell, A. K.; Del Sesto, R. E. Improved hydrogen release from ammonia-borane with ZIF-8. Inorg. Chem. 2012, 51 (5), 2728-2730. DOI: 10.1021/ic202562b.

(8) Hoon, C. F.; Reynhardt, E. C. Molecular dynamics and structures of amine boranes of the type $R_3N.BH_3$. I. X-ray investigation of $H_3N.BH_3$ at 295 K and 110 K. Journal of Physics C: Solid State Physics 1983, 16 (32), 6129-6136. DOI: 10.1088/0022-3719/16/32/007.

(9) Yang, J. B.; Lamsal, J.; Cai, Q.; James, W. J.; Yelon, W. B. Structural evolution of ammonia borane for hydrogen storage. Appl. Phys. Lett. 2008, 92, 091916. DOI: 10.1063/1.2889535.

(10) Hess, N. J.; Schenter, G. K.; Hartman, M. R.; Daemen, L. L.; Proffen, T.; Kathmann, S. M.; Mundy, C. J.; Hartl, M.; Heldebrant, D. J.; Stowe, A. C.; et al. Neutron Powder Diffraction and Molecular Simulation Study of the Structural Evolution of Ammonia Borane from 15 to 340 K. J. Phys. Chem. A 2009, 113, 5723-5735. DOI: 10.1021/jp900839c.

(11) Klooster, W. T.; Koetzle, T. F.; Siegbahn, P. E. M.; Richardson, T. B.; Crabtree, R. H. Study of the N–H…H–B Dihydrogen Bond Including the Crystal Structure of BH_3NH_3 by Neutron Diffraction. Journal of the American Chemical Society 1999, 121 (27), 6337-6343. DOI: 10.1021/ja9825332.

(12) Bowden, M. E.; Gainsford, G. J.; Robinson, W. T. Room-Temperature Structure of Ammonia Borane. Aust. J. Chem. 2007, 60 (3). DOI: 10.1071/ch06442.

(13) Morrison, C. A.; Siddick, M. M. Dihydrogen bonds in solid BH_3NH_3. Angew. Chem. Int. Ed. Engl. 2004, 43 (36), 4780-4782. DOI: 10.1002/anie.200460096.

(14) Mo, Y.; Song, L.; Wu, W.; Zhang, Q. Charge Transfer in the Electron Donor-Acceptor Complex BH_3NH_3. Journal of the American Chemical Society 2004, 126, 3974-3982. DOI: 10.1021/ja039778l.

(15) Yao, Y.; Yong, X.; Tse, J. S.; Greschner, M. J. Dihydrogen Bonding in Compressed Ammonia Borane and Its Roles in Structural Stability. The Journal of Physical Chemistry C 2014, 118 (51), 29591-29598. DOI: 10.1021/jp509633h.

(16) Yamauchi, K.; Hamada, I.; Huang, H.; Oguchi, T. Role of van der Waals interaction in crystalline ammonia borane. Appl. Phys. Lett. 2011, 99 (18). DOI: 10.1063/1.3657526.

(17) Walsh, A.; Sokol, A. A.; Buckeridge, J.; Scanlon, D. O.; Catlow, C. R. A. Electron Counting in Solids: Oxidation States, Partial Charges, and Ionicity. J Phys Chem Lett 2017, 8 (9), 2074-2075. DOI: 10.1021/acs.jpclett.7b00809.

(18) Sears, V. F. Neutron scattering lengths and cross sections. Neutron News 1992, 3, 26-37. DOI: 10.1080/10448639208218770.

(19) Egami, T.; Billinge, S. J. L. Underneath the Bragg Peaks:Structural Analysis of Complex Materials. Pergamon Materials Series 2012, 16, 2–481.

(20) Oishi, R.; Yonemura, M.; Nishimaki, Y.; Torii, S.; Hoshikawa, A.; Ishigaki, T.; Morishima, T.; Mori, K.; Kamiyama, T. Rietveld analysis software for J-PARC. Nucl. Instrum. Methods Phys. Res. A 2009, 600 (1), 94–96. DOI: 10.1016/j.nima.2008.11.056.

(21) Oishi-Tomiyasu, R. Rapid Bravais-lattice determination algorithm for lattice parameters containing large observation errors. Acta Crystallogr. A 2012, 68, 525–535. DOI: 10.1107/S0108767312024579.

(22) Keen, D. A. A comparison of various commonly used correlation functions for describing total scattering. J. Appl. Crystallogr. 2001, 34, 172–177. DOI: 10.1107/S0021889800019993.

(23) Ohara, K.; Tominaka, S.; Yamada, H.; Takahashi, M.; Yamaguchi, H.; Utsuno, F.; Umeki, T.; Yao, A.; Nakada, K.; Takemoto,

M.; et al. Time-resolved pair distribution function analysis of disordered materials on beamlines BL04B2 and BL08W at SPring-8. J Synchrotron Radiat 2018, 25 (Pt 6), 1627-1633. DOI: 10.1107/S1600577518011232.
(24) Farrow, C. L.; Juhas, P.; Liu, J. W.; Bryndin, D.; Bozin, E. S.; Bloch, J.; Proffen, T.; Billinge, S. J. PDFfit2 and PDFgui: computer programs for studying nanostructure in crystals. J. Phys.: Condens. Matter 2007, 19 (33), 335219-335211–335217. DOI: 10.1088/0953-8984/19/33/335219.
(25) Toby, B. H.; Von Dreele, R. B. GSAS-II: the genesis of a modern open-source all purpose crystallography software package. J. Appl. Crystallogr. 2013, 46 (2), 544–549. DOI: 10.1107/s0021889813003531.
(26) Tucker, M. G.; Keen, D. A.; Dove, M. T.; Goodwin, A. L.; Hui, Q. RMCProfile: reverse Monte Carlo for polycrystalline materials. J. Phys. Condens. Matter 2007, 19 (33), 335218. DOI: 10.1088/0953-8984/19/33/335218.
(27) Kresse, G.; Hafner, J. Ab initio molecular dynamics for liquid metals. Phys. Rev. B: Condens. Matter 1993, 47 (1), 558–561. DOI: 10.1103/physrevb.47.558.
(28) Kresse, G.; Furthmüller, J. Efficient iterative schemes for ab initio total-energy calculations using a plane-wave basis set. Phys. Rev. B: Condens. Matter 1996, 54, 11169–11186. DOI: 10.1103/PhysRevB.54.11169.
(29) Blöchl, P. E. Projector augmented-wave method. Phys. Rev. B: Condens. Matter 1994, 50 (24), 17953–17979. DOI: 10.1103/physrevb.50.17953.
(30) Kresse, G.; Joubert, D. From ultrasoft pseudopotentials to the projector augmented-wave method. Phys. Rev. B: Condens. Matter 1999, 59, 1758–1770. DOI: 10.1103/PhysRevB.59.1758.
(31) Perdew, J. P.; Burke, K.; Ernzerhof, M. Generalized Gradient Approximation Made Simple. Phys. Rev. Lett. 1996, 77 (18). DOI: 10.1103/PhysRevLett.77.3865.
(32) Palumbo, O.; Paolone, A.; Rispoli, P.; Cantelli, R.; Autrey, T.; Karkamkar, A.; Navarra, M. A. Hydrogen isotope effects on the structural phase transition of NH3BH3. Int. J. Hydrogen Energy 2011, 36 (13), 7927-7931. DOI: 10.1016/j.ijhydene.2010.12.076.
(33) Hess, N. J.; Bowden, M. E.; Parvanov, V. M.; Mundy, C.; Kathmann, S. M.; Schenter, G. K.; Autrey, T. Spectroscopic studies of the phase transition in ammonia borane: Raman spectroscopy of single crystal NH_3BH_3 as a function of temperature from 88 to 330 K. J. Chem. Phys. 2008, 128 (3), 034508. DOI: 10.1063/1.2820768 .
(34) Ikeda, K.; Ohshita, H.; Otomo, T.; Sakaki, K.; Kim, H.; Nakamura, Y.; Machida, A.; Von Dreele, R. B. Pressure cells for in situ neutron total scattering: time and real-space resolution during deuterium absorption. J. Appl. Crystallogr. 2022, 55 (6), 1631–1639. DOI: 10.1107/s1600576722010561.
(35) Stowe, A. C.; Shaw, W. J.; Linehan, J. C.; Schmid, B.; Autrey, T. In situ solid state 11B MAS-NMR studies of the thermal decomposition of ammonia borane: mechanistic studies of the hydrogen release pathways from a solid state hydrogen storage material. Phys. Chem. Chem. Phys. 2007, 9 (15), 1831-1836. DOI: 10.1039/b617781f.
(36) Shaw, W. J.; Linehan, J. C.; Szymczak, N. K.; Heldebrant, D. J.; Yonker, C.; Camaioni, D. M.; Baker, R. T.; Autrey, T. In situ multinuclear NMR spectroscopic studies of the thermal decomposition of ammonia borane in solution. Angew. Chem. Int. Ed. Engl. 2008, 47 (39), 7493-7496. DOI: 10.1002/anie.200802100.
(37) Momma, K.; Izumi, F. VESTA 3for three-dimensional visualization of crystal, volumetric and morphology data. J. Appl. Crystallogr. 2011, 44 (6), 1272-1276. DOI: 10.1107/s0021889811038970.
(38) Henkelman, G.; Arnaldsson, A.; Jónsson, H. A fast and robust algorithm for Bader decomposition of charge density. Computational Materials Science 2006, 36 (3), 354-360. DOI: 10.1016/j.commatsci.2005.04.010.
(39) Gjerding, M. N.; Taghizadeh, A.; Rasmussen, A.; Ali, S.; Bertoldo, F.; Deilmann, T.; Knøsgaard, N. R.; Kruse, M.; Larsen, A. H.; Manti, S.; et al. Recent progress of the Computational 2D Materials Database (C2DB). 2D Materials 2021, 8 (4). DOI: 10.1088/2053-1583/ac1059.
(40) Wu, C.; Wu, G.; Xiong, Z.; Han, X.; Chu, H.; He, T.; Chen, P. $LiNH_2BH_3{\cdot}NH_3BH_3$: Structure and Hydrogen Storage Properties. Chem. Mater. 2009, 22 (1), 3-5. DOI: 10.1021/cm903167b.
(41) Shimoda, K.; Doi, K.; Nakagawa, T.; Zhang, Y.; Miyaoka, H.; Ichikawa, T.; Tansho, M.; Shimizu, T.; Burrell, A. K.; Kojima, Y. Comparative Study of Structural Changes in NH_3BH_3, $LiNH_2BH_3$, and KNH_2BH_3 During Dehydrogenation Process. The Journal of Physical Chemistry C 2012, 116 (9), 5957-5964. DOI: 10.1021/jp212351f.
(42) Xiong, Z.; Yong, C. K.; Wu, G.; Chen, P.; Shaw, W.; Karkamkar, A.; Autrey, T.; Jones, M. O.; Johnson, S. R.; Edwards, P. P.; et al. High-capacity hydrogen storage in lithium and sodium amidoboranes. Nat Mater 2008, 7 (2), 138-141. DOI: 10.1038/nmat2081.
(43) Himmelberger, D. W.; Yoon, C. W.; Bluhm, M. E.; Carroll, P. J.; Sneddon, L. G. Base-promoted ammonia borane hydrogen-release. J. Am. Chem. Soc. 2009, 131 (39), 14101-14110. DOI: 10.1021/ja905015x.
(44) Lee, T. B.; McKee, M. L. Mechanistic study of $LiNH_2BH_3$ formation from $(LiH)_4 + NH_3BH_3$ and subsequent dehydrogenation. Inorg. Chem. 2009, 48 (16), 7564-7575. DOI: 10.1021/ic9001835.
(45) Miwa, K.; Sato, T.; Matsuo, M.; Ikeda, K.; Otomo, T.; Deledda, S.; Hauback, B. C.; Li, G.; Takagi, S.; Orimo, S.-i. Metallic Intermediate Hydride Phase of $LaMg_2Ni$ with Ni–H Covalent Bonding: Precursor State for Complex Hydride Formation. The Journal of Physical Chemistry C 2016, 120 (11), 5926-5931. DOI: 10.1021/acs.jpcc.6b00341.
(46) Sato, T.; Ikeda, K.; Matsuo, M.; Miwa, K.; Otomo, T.; Deledda, S.; Hauback, B. C.; Li, G.; Takagi, S.; Orimo, S.-i. In-situ powder neutron diffraction study on the formation process of $LaMg_2NiH_7$. Int. J. Hydrogen Energy 2017, 42 (35), 22449-22453. DOI: 10.1016/j.ijhydene.2017.02.196.